Supplemental Document

Chiral topological add–drop filter for integrated quantum photonic circuits: supplement

M. Jalali Mehrabad,[1,2,5] A. P. Foster,[1,3] N. J. Martin,[1,*] R. Dost,[1] E. Clarke,[4] P. K. Patil,[4] M. S. Skolnick,[1] and L. R. Wilson[1]

[1] *Department of Physics and Astronomy, University of Sheffield, Sheffield S3 7RH, UK*
[2] *Current address: Joint Quantum Institute, University of Maryland, College Park, Maryland 20742, USA*
[3] *Current address: Aegiq Ltd, Cooper Buildings, Arundel Street, Sheffield S1 2NS, UK*
[4] *EPSRC National Epitaxy Facility, University of Sheffield, Sheffield S1 4DE, UK*
[5] *mjalalim@umd.edu*
[*] *nmartin3@sheffield.ac.uk*

Supplement DOI: https://doi.org/10.6084/m9.figshare.22025564

Parent Article DOI: https://doi.org/10.1364/OPTICA.481684

Supporting Information for: A chiral topological add-drop filter for integrated quantum photonic circuits

M. Jalali Mehrabad,[1,*] A.P. Foster,[1,†] N.J. Martin,[1,‡] R. Dost,[1]
E. Clarke,[2] P.K. Patil,[2] M.S. Skolnick,[1] and L.R. Wilson[1]

[1] *Department of Physics and Astronomy, University of Sheffield, Sheffield S3 7RH, UK*
[2] *EPSRC National Epitaxy Facility, University of Sheffield, Sheffield S1 4DE, UK*

This file contains supporting information for the paper "A chiral topological add-drop filter for integrated quantum photonic circuits".

CONTENTS

* mjalalim@umd.edu; Current address: Joint Quantum Institute, University of Maryland, College Park, MD 20742, USA
† Current address: Aegiq Ltd, Cooper Buildings, Arundel Street, Sheffield, S1 2NS, UK
‡ nmartin3@sheffield.ac.uk

S1. MODE PROFILES AND CHIRAL SPATIAL MAPS FOR THE TOPOLOGICAL INTERFACE.

Fig. S1 shows the electric field intensity distribution of the guided mode for the type A and type B valley-Hall zigzag topological interfaces, as introduced in Fig. 1 of the main text. Also shown in each case is the normalised Stokes S_3 parameter (degree of circularity) for the same cross-section of the waveguide. This is otherwise known as a chiral map, with regions of $|S_3| \to 1$ suppporting chiral coupling of an embedded emitter with circularly polarised transition dipole moment. Using the fields obtained from finite-difference time-domain (FDTD) simulations, the S_3 parameter was obtained from the expression

$$S_3 = \frac{-2\mathrm{Im}(E_x E_y^*)}{|E_x|^2 + |E_y|^2}, \tag{S1}$$

where S_3, E_x and E_y are dependent on x and y, with $z = 0$ (corresponding to the centre of the PhC membrane).

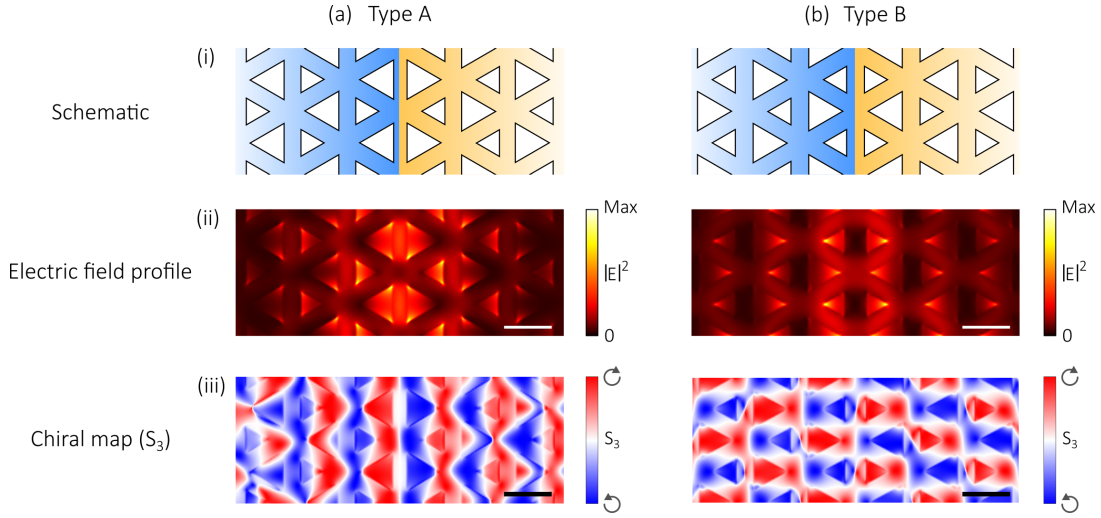

FIG. S1. Mode profiles and chiral maps for (a) type A and (b) type B valley-Hall zigzag topological interfaces, respectively. In each case (i) shows a schematic of the interface, (ii) gives the electric field intensity spatial map of the guided mode and (iii) shows the (normalised) S_3 Stokes parameter, giving the degree of circular polarisation of the mode as a function of (x, y) position. Scale bars in (b,c) are 200nm.

S2. CONTROL OF ADF COUPLING STRENGTH USING WAVEGUIDE-RESONATOR SEPARATION.

Here, we demonstrate control of the the add-drop filter (ADF) coupling strength at the design stage. To do so, we vary the waveguide-resonator separation S while keeping the parameters T and L constant (see Fig. S2a). By setting $S = 10, 6$ or 2 unit cells, the ring resonator and the bus and drop waveguides can be weakly, critically or over coupled, respectively. This is demonstrated in Fig. S2b, in which FDTD simulations are used to evaluate the time-averaged electric field intensity when light, resonant with the same longitudinal mode in each case, is injected into the drop waveguide of the ADF.

Next, we experimentally investigate structures with these same parameters using integrated photoluminescence (PL) intensity raster scans; the results are shown in Fig. S2d. For each of the three devices, we position the collection spot above the lower left outcoupler (OC) and raster scan the excitation laser across the device, as shown in Fig. S2c (this is the reverse of the collection raster scan used in the main text). By virtue of the spatially distributed nature of the QD ensemble, this approach effectively provides a user-positioned broadband light source with which to probe the optical response of the device. We integrate the measured PL intensity over a bandwidth corresponding to the same resonator mode in each case.

For $S = 10$, light from the drop waveguide weakly couples to the ring, and we see emission which originates from both waveguides, and from within the resonator. For the $S = 6$ case, in which the the mode is near-critically coupled, light is seen to couple through the resonator from the drop (upper) waveguide, while light from the other ends of the drop or through waveguides is not detected. This light is instead coupled via the resonator to the OC on the right hand side of the bus waveguide, in a mirror image of the data shown here. Finally, when $S = 2$, the resonator is overly coupled to the waveguides. In this scenario, the light coupled from the drop waveguide to the ring subsequently couples quickly to the bus waveguide.

Note that the approaches used to obtain the simulation data in Fig. S2b and experimental data in Fig. S2d are not directly equivalent; nevertheless, in combination they clearly demonstrate how changing the parameter S changes the resonator-waveguide coupling strength.

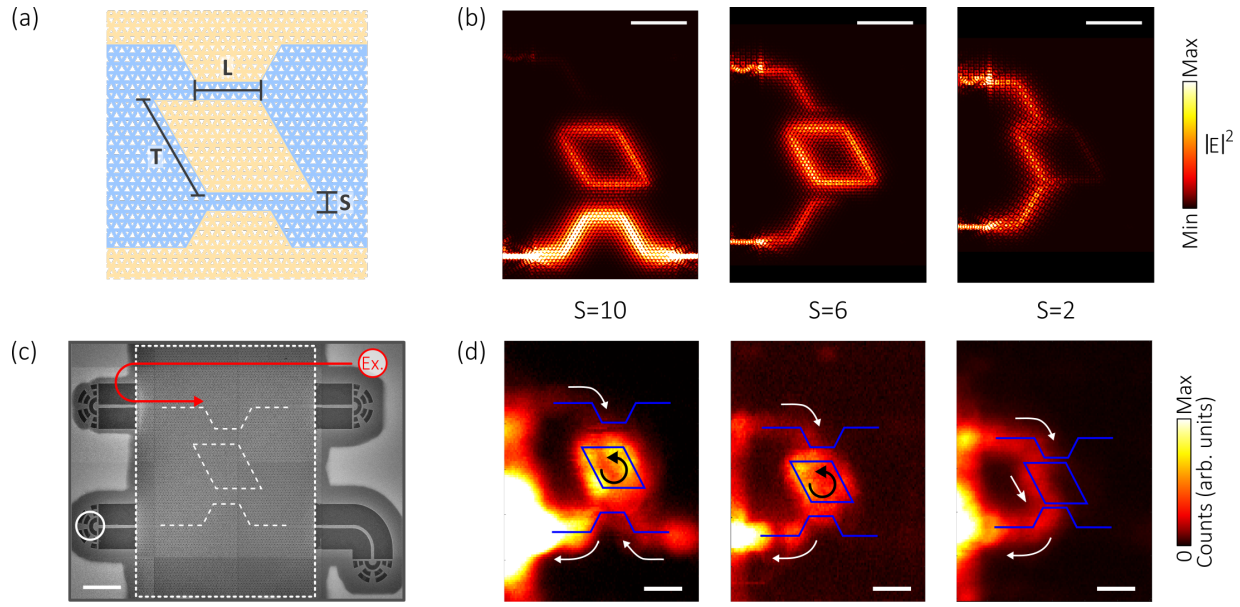

FIG. S2. Control of ADF coupling strength by changing the waveguide-resonator separation. (a) Schematic of the ADF. (b) Time-averaged electric field intensity spatial maps for three ADFs with different waveguide-resonator separation (from left to right, S=10, 6 and 2 unit cells, respectively). In each case, light which is resonant with a single longitudinal mode of the resonator is injected into the bottom left waveguide. (c) SEM of an ADF. Ex. - excitation spot location. (d) Integrated PL intensity spatial maps for devices with (left to right) S=10, 6 and 2 unit cells. PL is collected from the OC terminating the lower left output port, while the excitation laser spot is rastered across the device (indicated by the red arrow in (c)). In each case, the integration is taken over a single longitudinal mode at $\sim$ 1000nm. Solid blue lines give the positions of the waveguides and resonator. White and black arrows indicate the dominant direction of power flow. Scale bars in (b,c) are 4μm.

S3. VALLEY MOMENTUM CONSERVATION IN THE ADF.

The direction in which light propagates in the ADF depends on the interface type (A or B) and is dictated by valley momentum conservation [1]. This can be understood by considering the phase winding of the H_z field at the K and K' points in the Brillouin zone, and the dependence of the winding direction on the orientation of the PhC unit cell (and therefore the interface type). In Fig. S3a we plot the phase of the H_z field for the lowest frequency TE mode at the K and K' points, for both VPC1 and VPC2 PhCs. (The phase was obtained using the freely available MIT Photonic Bands (MPB) software package [2].) For a PhC formed using VPC1 unit cells, the phase at the K point winds by 2π in the clockwise (CW) direction about the centre point. When the unit cells are inverted (i.e. the PhC becomes VPC2-type) the phase rotates in the counter-clockwise (CCW) direction. Conversely, at the K' point the opposite behaviour is observed.

A type A interface is now formed by positioning a VPC1 PhC above a VPC2 PhC (i.e. separated in the y direction), with the resulting waveguide oriented along the x direction (see schematic 1 in Fig. S3b). At the K' point, the field vortices indicate that the interface mode will propagate in the positive x direction. Conversely, for a type B interface the VPC2 PhC is positioned above the VPC1 PhC, and the field vortices are therefore reversed. The K' interface mode in this case propagates in the negative x direction (see schematic 4 in Fig. S3b).

Within the ADF, there are six different combinations of interface type (A or B) and direction (inclined at 0, 60 or 120 degrees to the x axis). However, these can all be traced back to one of the two scenarios outlined above, by a suitable rotation of the waveguide. For instance, the interfaces in schematics 1, 2 and 3 in Fig. S3b are equivalent

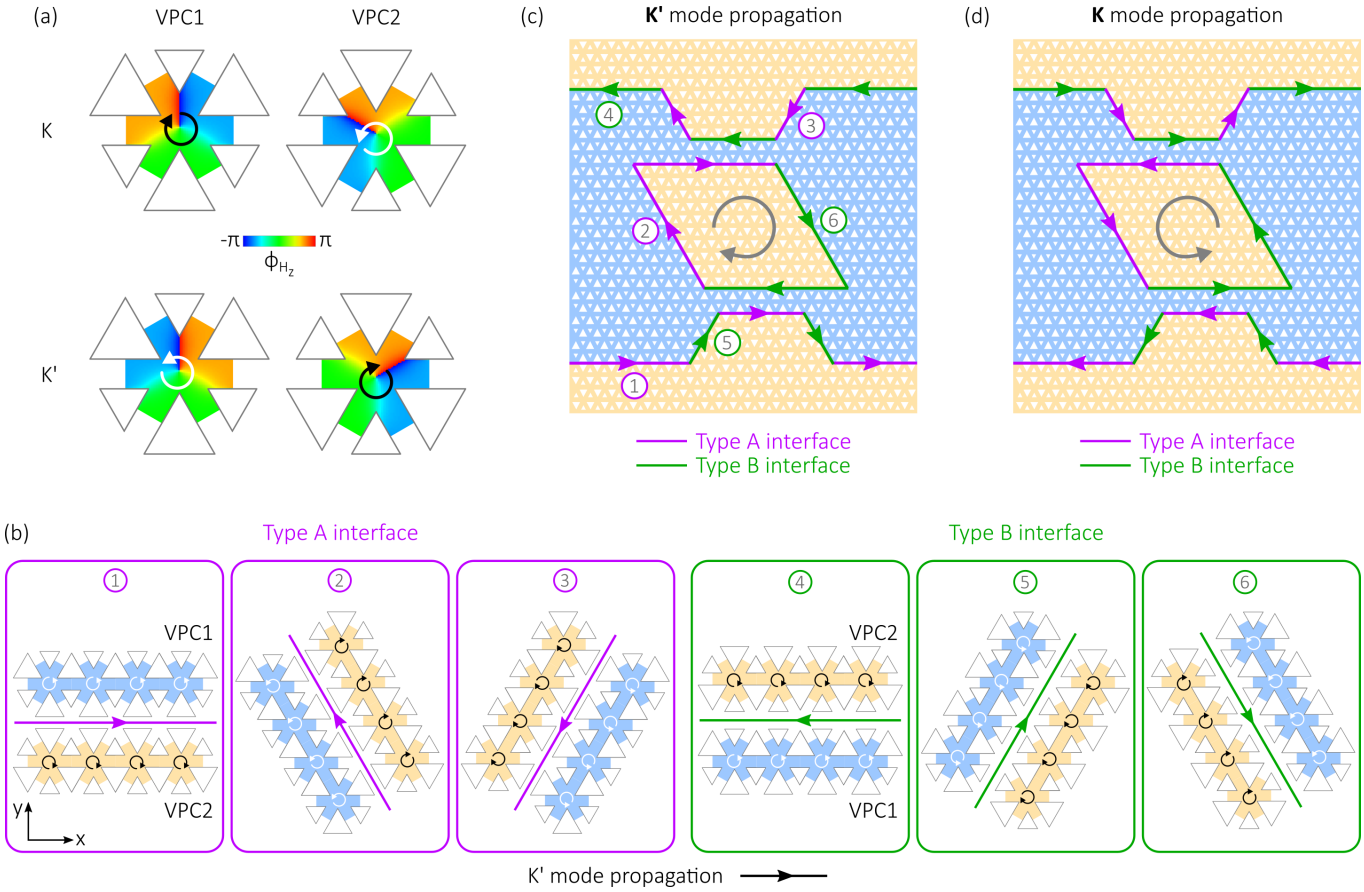

FIG. S3. (a) Phase vortices for the H_z field at the K and K' points of the lowest frequency TE band, for PhCs formed using either inverted (VPC1) or uninverted (VPC2) unit cells. (b) Schematic showing the direction of light propagation within the K' mode for the six possible combinations of interface type and waveguide orientation in the topological PhC. The phase vortices for the VPC1 and VPC2 unit cells are given by white and black circular arrows, respectively. Straight arrows for the type A and B interface propagation directions are coloured purple and green, respectively. Waveguides 1, 2 and 3 are equivalent, differing only by rotation; the same is true for waveguides 4, 5 and 6. All arrows are inverted for propagation in the K direction. (c,d) Schematic showing the direction of light propagation within the (c) K' or (d) K mode of an ADF.

other than by a rotation. The same is true for the interfaces labelled 4, 5 and 6. Using this basis, we indicate on a schematic of the ADF in Fig. S3c the direction of propagation for the K' mode. If light is injected into the right travelling mode in the bus (lower) waveguide, a CW resonator mode is subsequently excited; this decays into the left travelling mode in the drop (upper) waveguide. The reversed situation for the K mode is shown in Fig. S3d.

Using the above considerations, if light is injected into the K mode in the bus waveguide (i.e. propagating from right to left), transmission into the left travelling K' mode in the drop waveguide should be inhibited, as this necessitates flipping of the k-vector. In Fig. 3f of the main text, this suppression of coupling into the 'wrong' mode of the experimental drop waveguide is clearly seen.

Note also that topological protection should result in suppression of reflection by the ADF, as this also necessitates flipping of the k-vector. An observation along these lines has been made recently in an elastic wave spin-Hall system [3], in which topological protection prohibits quasi-spin flips.

S4. DEFECT ROBUSTNESS OF THE ADF.

Here, we use FDTD simulations to demonstrate the robustness of the ADF against certain defects. We first consider defects formed by the omission of either a single small or large triangle at the resonator interface, for either a type A or type B interface. Then, we look at the effect of perturbing the size of a subset of unit cells at the resonator interface. To reduce computational demand, we utilise the '2.5D' varFDTD solver provided by Lumerical's MODE Solutions software. This is a two-dimensional solver in which the properties of the third dimension are approximated using an effective refractive index, typically resulting in a dispersive material index. In our simulations this approximation leads to a shift in wavelength and reduction in bandwidth of the photonic bandgap compared with a full 3D simulation. However, we have confirmed that the trends revealed are faithful to the 3D system. In particular, we find that the three resonator modes obtained using the 2.5D approach correspond to the three longest wavelength modes in 3D simulations.

The simulated through and drop signals when a triangle is omitted from the resonator interface are shown in Fig. S4. In each case the unperturbed result is also shown for reference. Small triangle defects are seen to have a minor effect on the device transmission, other than for the shortest wavelength mode when the defect is at a type B interface. Omission of a large triangle has a slightly larger impact, as shown in Fig. S4c,d. Additional sharp features also arise in the spectra in cases b-d, due to localisation within the respective defects.

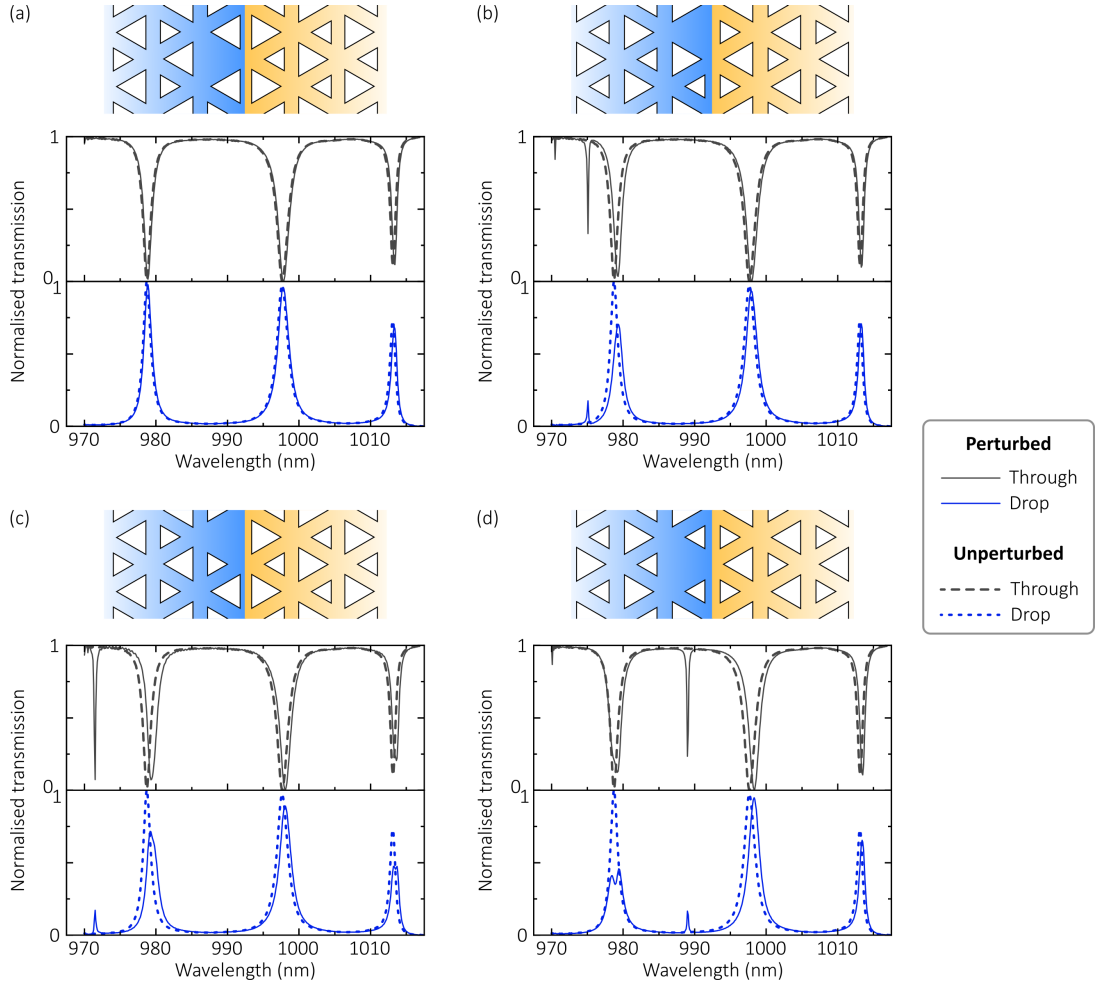

FIG. S4. Simulated through (middle panel) and drop (lower panel) spectra for ring resonators having a single interface defect. The defect takes the form of an omitted small triangle at an (a) type A or (b) type B interface, or an omitted large triangle at a (c) type A or (d) type B interface, as shown schematically in the upper panel in each case.

Next, we consider a perturbation consisting of a change in size of the triangles forming 6 neighbouring unit cells, three on either side of the type B resonator interface (the results are similar for the type A interface). The perturbation is shown schematically in Fig. S5a, and the resulting through and drop spectra shown in Fig. S5b,c. Other than a

mode wavelength shift, the spectra are almost unchanged when compared with the unperturbed case.

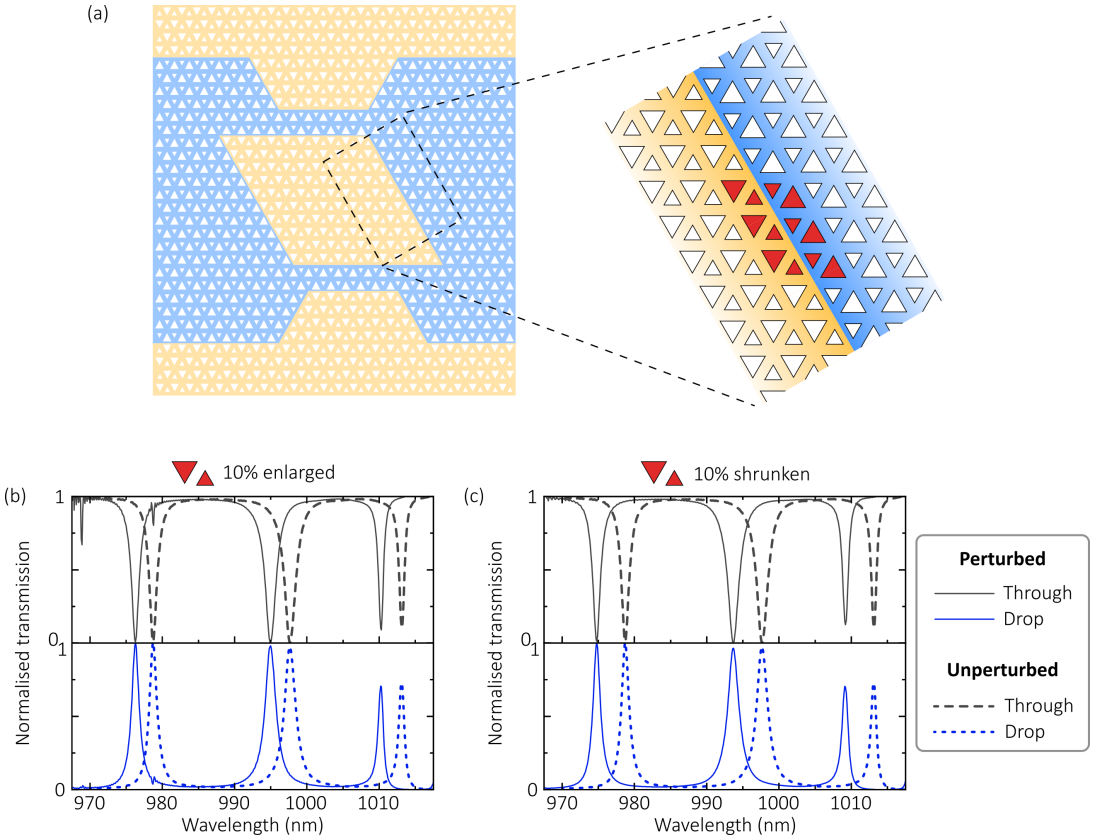

FIG. S5. (a) Schematic of the ADF. The unit cells shaded in red are modified in (b,c). (b,c) Simulated through and drop spectra for an ADF in which the sizes of the triangles within the filled red unit cells in (a) are changed by (b) +10% and (c) -10%. The unperturbed spectra are also shown for reference. The simulated ADF has $T = 16$, $S = 8$ and $L = 11$ unit cells, respectively, as defined in the main text.

S5. LOGIC GATE OPERATION AND ROBUSTNESS

The combination of topological resonator and twin access waveguides supports applications beyond the add-drop filter. The same configuration can be used, for instance, as the basis for many distinct all-optical logic gates, with applications in optical computing and signal processing. As an example of this multi-functionality, we present simulations for a combined XOR/OR logic gate, and demonstrate robustness of the device against specific resonator defects. (Note that other major logic gates such as AND, NOT and NOR gates may also be realised using the same principles.) The XOR/OR gate takes two inputs A and B, with the input state given by $i_A i_B$, where $i = 1(0)$ in the presence (absence) of the relevant input. In our simulations, the inputs are provided by chiral sources located in the lower left and upper right access waveguides, respectively (inputs A and B in Fig. S6a). The XOR and OR output states of the gate are defined as 1(0) in the presence (absence) of an electric field at the XOR and OR output waveguides, respectively.

We operate the gate at a wavelength corresponding to 50% coupling efficiency between the access waveguides and ring resonator. By controlling the input phases and amplitudes, an XOR output of 1 can be obtained if either (but not both) of the inputs is present; this is due to destructive interference occurring in the XOR output waveguide when both inputs are present [4]. This can be seen in Fig. S6b, in which the transmission into the XOR output is plotted as a function of wavelength for one longitudinal mode of the resonator. The accompanying electric field profiles (Fig. S6d-f) show the absence of a field in the XOR output only in the case of a 11 input. At the same time, at the OR output constructive interference occurs for a 11 input (Fig. S6c), thus ensuring an output of 1 when any non-zero input is present. We note that this form of logic gate was previously proposed for the topological photonic spin-Hall system [4], an approach subject to considerably larger transmission losses than the valley-Hall system we consider here.

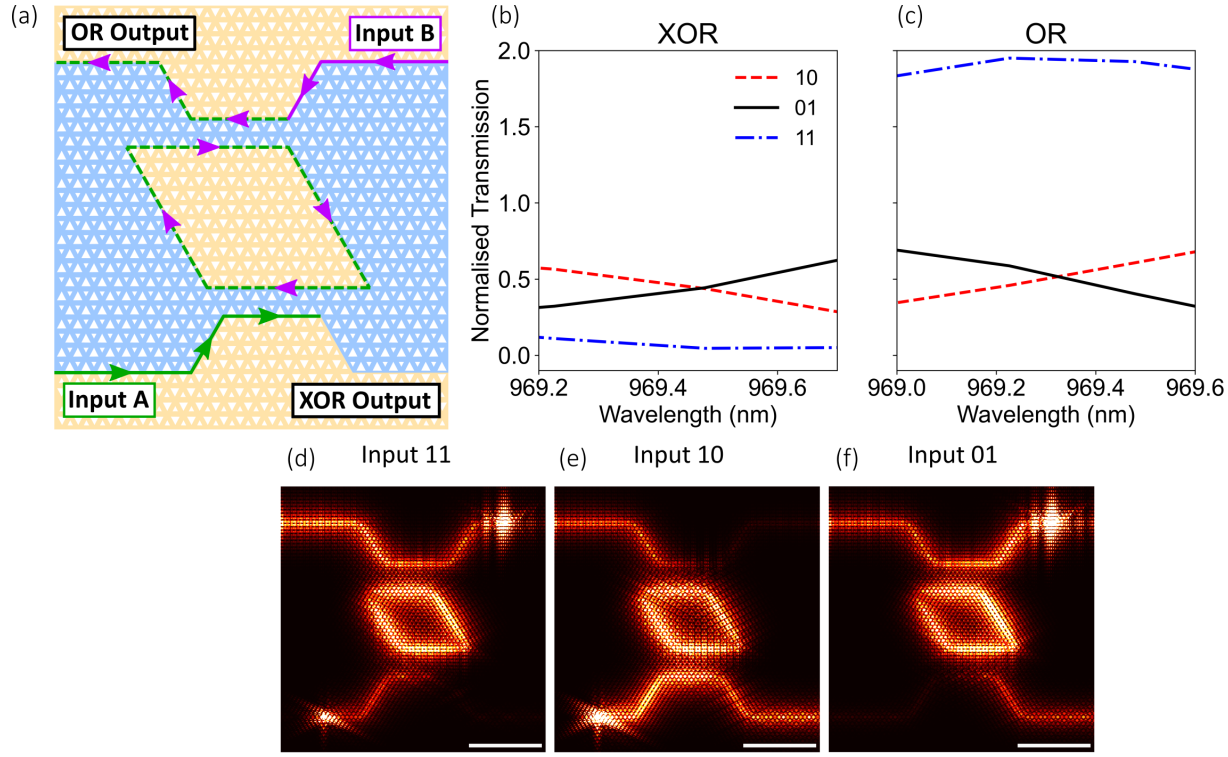

FIG. S6. (a) Schematic of the combined XOR/OR logic gate, with inputs A and B and outputs XOR and OR. The simulated device has design parameters of S=8, T=17 and L=15 (see Fig. S2a). (b-c) Normalised transmission into the (b) XOR and (c) OR output ports, respectively, for inputs 01, 10 or 11. Note that the normalisation is undertaken with respect to a single input. (d-f) Time-averaged electric field intensity spatial maps for inputs (d) 11, (e) 10 and (f) 01, respectively. Here, an electric field at an output port signifies an output of 1 while the absence of a field corresponds to an output of 0. Scale bars in (d-f) are 4μm.

To demonstrate the robust operation of the logic gate we investigate two perturbations to the original design. Specifically, we consider (i) removal of holes from near the waveguide interface of the ring resonator and (ii) swapping type A and type B unit cells at the same interface. In each case, Fig. S7 shows the time-averaged electric field spatial

maps for the 11 input state, as well as a comparison with the unmodified design.

For case (i), we consider the failure of a small feature to transfer during fabrication from the electron beam resist into the semiconductor membrane. This is a relatively common defect resulting from nanofabrication imperfections, for instance due to a local defect in the lithography resist. Two such perturbations are shown in Fig. S7(c-d), with the missing feature in each case highlighted by a dashed triangle. Despite the presence of the defect, the XOR(OR) output state remains 0(1), as in the unperturbed case. This implies that devices with such missing holes operate without significant additional back-scatter.

In case (ii), we exchange up to six unit cells at the resonator interface (by swapping type A cells with type B). Fig. S7(e-f) shows the results for both one and six exchanged unit cells. Once again, the device performance is unchanged relative to the unperturbed device. This is possible because the the path length of the resonator under unit cell exchange is largely unchanged (significant changes to the path length would alter the relative phase of the two inputs, and therefore their interference). The topological ADF is therefore a versatile design, with structures of varying geometries being viable. This is particularly useful when integrating randomly positioned emitters such as quantum dots into resonator devices, as the emitters can be located prior to fabrication (using registration techniques), and devices of suitable geometry formed around them.

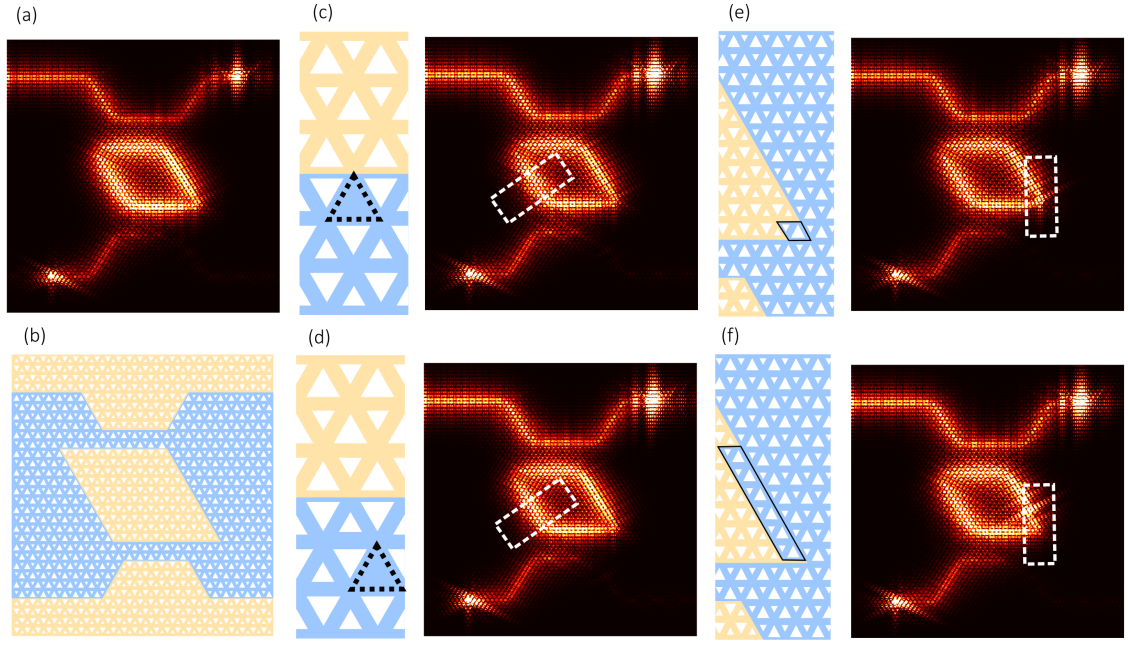

FIG. S7. Time-averaged electric field intensity spatial maps at 969.3nm of XOR/OR operation with a 11 input for different defects and distortions of the ring resonator. (a-b) Original unaltered design. (c-d) Gate with a singular smaller hole removed one and two lattice constants away from the ring resonator interface respectively. (e-f) Gates with Distortions to the ring resonator through swapping the unit cells of one photonic crystal for the other.

S6. EXCITATION PL SPATIAL MAPPING.

In addition to the collection raster scans shown in in Fig. 3 of the main text, we have performed excitation raster scans on the same device. In this complementary measurement, we position the collection above the bottom right OC and raster scan the excitation laser across the device (the reverse of the collection raster scan shown in the main text). When the PL emission is spectrally filtered such that the emission energy is off-resonance with the mode, the (integrated) PL is seen to originate only from the through waveguide (Fig. S8c). In this scenario, the resonator and waveguide modes are decoupled. On resonance, however, light is detected which originates either from one end of the drop waveguide (i.e. coupled through the resonator), or from within the resonator itself (Fig. S8b). As the mode is near-critically coupled, light from the other ends of the drop or through waveguides is not detected. This light is instead coupled via the resonator to the OCs on the left hand side of the device, in a mirror image of the data shown here.

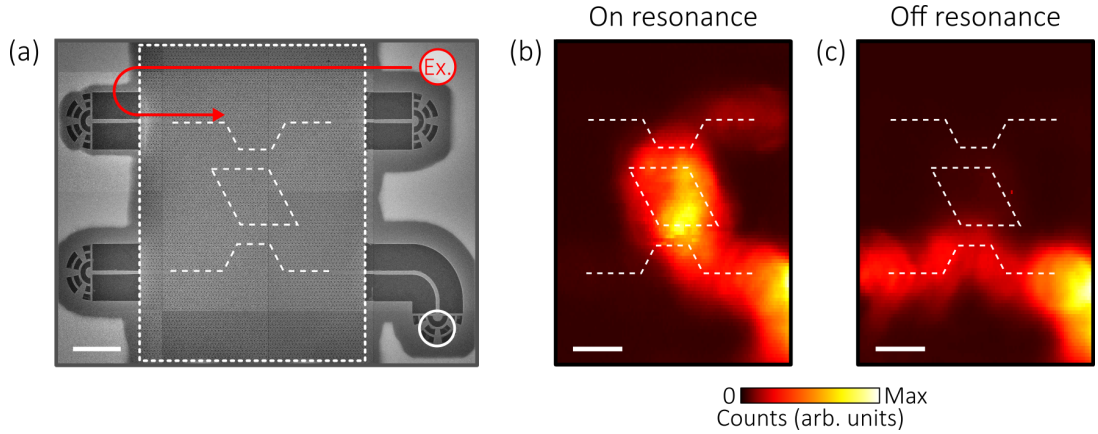

FIG. S8. (a) SEM of an ADF. Ex. - excitation spot location, which is rastered across the device. (b, c) Integrated PL intensity as a function of excitation position, for the device shown in Figure 3 of the main text. PL is collected from the OC terminating the lower right OC (white circle in (a)), while the excitation laser spot is rastered across the device. The integration is taken over (b) 939.3nm to 939.5nm or (c) 943nm to 944nm. Dashed white lines give the positions of the waveguides and resonator. The area shown in the maps corresponds to the dotted white box in (a). Scale bars in (a-c) are 4μm.

S7. ADF AS A SINGLE PHOTON BEAMSPLITTER FOR AUTOCORRELATION MEASUREMENTS.

Second order autocorrelation measurements (or Hanbury-Brown and Twiss (HBT) measurements) are a standard technique to demonstrate single photon emission from a quantum emitter such as a QD. Typically, one collects photons emitted by the QD and directs them to a pair of single photon detectors via a 50:50 beamsplitter. For a perfect single photon source, correlations between arrival times of the photons show complete suppression at zero time delay. Here, we use the add-drop filter itself as an on-chip beamsplitter. An SEM of the device is shown in Fig. S9a. First, we identify the spectral position of resonator modes which are coupled to the bus waveguides. We probe the transmission of the lower bus waveguide by exciting ensemble PL from within the bottom right hand OC, detecting the signal from the bottom left hand OC. The resulting transmission spectrum is shown in Fig. S9b, with several clear dips observed due to waveguide-resonator coupling.

Next, we identify a QD located within the resonator and coupled to the mode at $\sim$ 952nm. Using low power non-resonant excitation ($\lambda_{\text{laser}} = 808$nm), we collect PL simultaneously from both ends of the lower bus waveguide, as indicated in the schematic in Fig. S9c. The QD couples to both CW and CCW resonator modes with similar efficiency, and the modes subsequently decay in either direction along the bus waveguide, thereby realising an approximately 50:50 beamsplitting operation. We filter the signal collected by both fibers using separate monochromators with $\sim$ 100pm filter bandwidth, with the signals prior to filtering shown in Fig. S9d. Note that due to the relatively high density of QDs in the sample, the filtered signal still contains a contribution from QDs other than the target QD transition. We then correlate the arrival times of photons from either collection fiber using a pair of APDs and time tagging electronics. The result of the HBT measurement is shown in Fig. S9e, with $g^{(2)}(0) = 0.53$ after deconvolution of the instrument response. If we then account for the signal to background ratio obtained from the filtered PL spectra, we obtain a corrected value of $g^{(2)}(0) = 0.14$, clearly demonstrating the single photon nature of the emission.

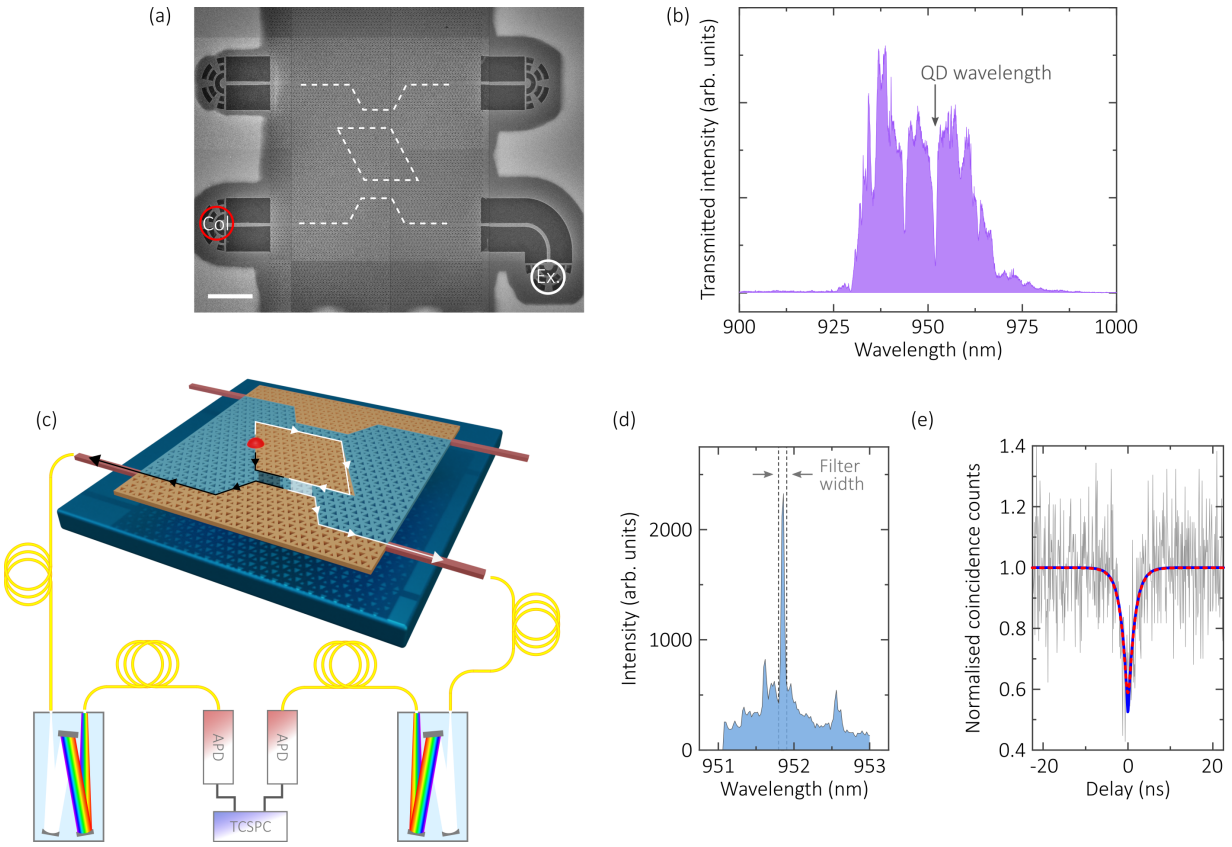

FIG. S9. (a) SEM of an ADF. Scale bar 4μm. (b) Transmitted PL spectrum acquired from the bottom left OC (red circle in (a)) after excitation of the QD ensemble in the bottom right OC. (c) Schematic of the HBT experimental setup. APD - avalanche photo diode; TCSPC - time correlated single photon counter. (d) PL spectra obtained from the left and right OCs of the waveguide in (c), respectively, when exciting a QD positioned at the resonator interface. The spectra are shown prior to spectral filtering. The QD transition is resonant with a cavity mode (arrow in (b)). (e) Second order auto-correlation measurement for the QD transition in (d). The red dashed line shows a convolved fit to the data, while the blue line shows the deconvolved fit, with $g^{(2)}(0) = 0.53$. The bin width is 100ps.

S8. BROADBAND NATURE OF CHIRAL COUPLING IN THE ADF.

Fig. S10 shows chiral coupling of a second QD to the device considered in Fig. 4 of the main text. Most importantly, note that the QD is coupled to a different mode of the resonator in this case. The QD is excited non-resonantly and PL emission is subsequently detected from the two ports on the right hand side of the ADF. The resulting spectra as a function of magnetic field are shown, clearly demonstrating routing of light dependent on the spin state of the QD transition.

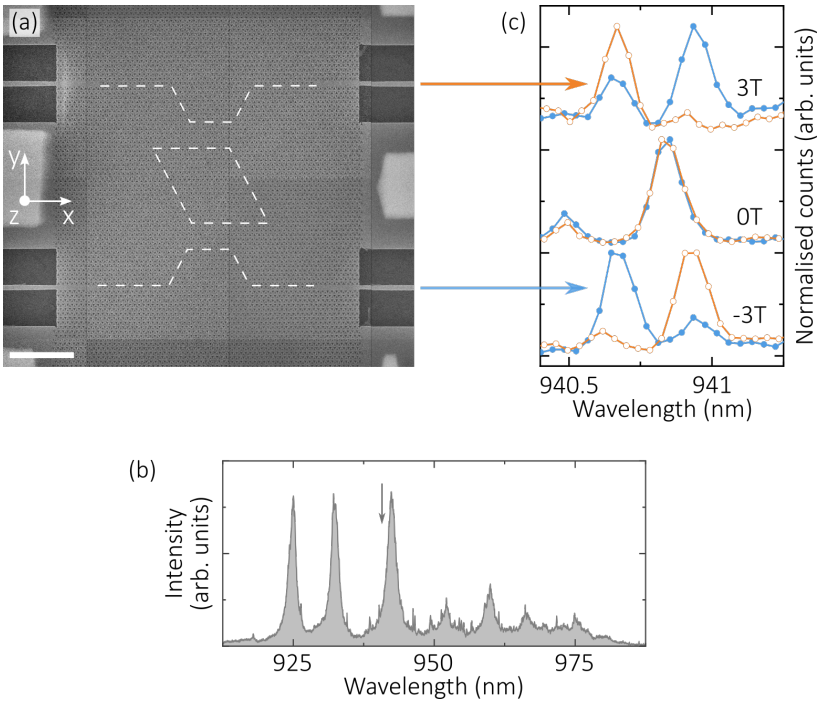

FIG. S10. SEM image of a representative ADF, with waveguide-resonator separation S=6 unit cells. Note that the measured device has S=10 unit cells. Dotted lines outline the waveguide and the resonator interfaces. Each nanobeam waveguide is terminated with an OC (not shown). Scale bar 4μm. (b) PL spectrum acquired from an OC under high-power excitation of the resonator interface. (c) Low power PL spectra for a single QD located at the resonator interface and with an optical transition near-resonant with a longitudinal mode (see arrow in (b)). The spectra are acquired from the OCs at the top right (orange line) and bottom right (blue line) of the device, respectively. Data is shown for three different magnetic field strengths, $B_z = -3$T, 0T and 3T, respectively.

[1] Y. Chen, X.-T. He, Y.-J. Cheng, H.-Y. Qiu, L.-T. Feng, M. Zhang, D.-X. Dai, G.-C. Guo, J.-W. Dong, and X.-F. Ren, Topologically protected valley-dependent quantum photonic circuits, Phys. Rev. Lett. **126**, 230503 (2021).
[2] S. G. Johnson and J. D. Joannopoulos, Block-iterative frequency-domain methods for Maxwell's equations in a planewave basis, Opt. Express **8**, 173 (2001).
[3] S.-Y. Yu, C. He, X.-C. Sun, H.-F. Wang, J.-Q. Wang, Z.-D. Zhang, B.-Y. Xie, Y. Tian, M.-H. Lu, and Y.-F. Chen, Critical couplings in topological-insulator waveguide-resonator systems observed in elastic waves, National Science Review **8**, 10.1093/nsr/nwaa262 (2020).
[4] L. He, W. X. Zhang, and X. D. Zhang, Topological all-optical logic gates based on two-dimensional photonic crystals, Opt. Express **27**, 25841 (2019).